Robust Lyapunov Control Design for Bioinspired Pursuit With Autonomous Hovercraft

Daigo Shishika, *Student Member, IEEE*, Justin K. Yim, and Derek A. Paley, *Senior Member, IEEE*

***Abstract*— The problem of pursuit has been studied mostly in the context of missile guidance and navigation; however, it is also an essential component in biological systems ranging from prey capture to mating and in bioinspired engineering applications with small agile vehicles. This paper considers the pursuit problem with a focus on robustness to noisy sensor measurements and efficiency in the control effort. We design a pursuit law based on Lyapunov analysis and establish its robustness to unknown target acceleration and measurement errors using the concept of ultimate boundedness. Robustness to control saturation is analyzed using the phase portrait of the closed-loop system. We also present results from experiments that were conducted to study the practical challenges involved in pursuit by lightweight platforms with noisy sensors. These experiments highlight the benefit of using less control effort in the presence of large measurement errors compared with existing pursuit guidance laws.**

***Index Terms*— Autonomous agents, control design, Lyapunov methods, missiles, nonlinear control systems, robust control.**

I. Introduction

HISTORICALLY, pursuit has been studied mainly for the purpose of missile guidance and navigation [1]–[7]. However, in this paper, we consider applications with small and agile systems such as microaerial vehicles (MAVs). Practical applications include drone countermeasures, i.e., tracking or intercepting a small multirotor helicopter using another multirotor helicopter.

In the missile-guidance literature, it has been shown that a viable approach to target intercept is stabilizing the line of sight (LOS) [1], i.e., the line extending from the pursuer to the target. A well-known strategy to achieve this approach is called proportional navigation (PN) [2]–[4]. Although PN requires more information about the target motion (such as LOS rate and range rate) than pure pursuit (also called classical pursuit [5]) in which the pursuer simply aims directly at the target, the efficiency of target intercept is enhanced by avoiding the tail-chase scenario [4]. PN is also known to have optimality in terms of the square integral of the control effort against a nonmaneuvering target [6].

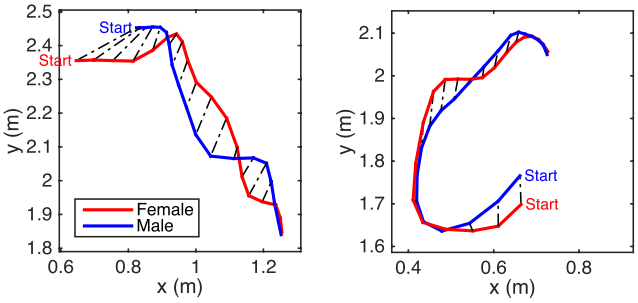

Fig. 1. Trajectories of wild mosquitoes in coupling flight, reconstructed from stereoscopic video sequences [12]. Pursuit (possibly mutual) continues after several close encounters.

To achieve LOS stabilization, various approaches have been taken with differing assumptions [2]–[7], including a nonmaneuvering target, constant-speed agents, linearized dynamics, initially negative range rate, and knowledge of the target's acceleration. However, these assumptions may not apply to systems that involve small and agile agents like MAVs.

Pursuit is also an important component in biological systems ranging from prey capture to mating [8]–[10]. Stabilization of the LOS has also been studied in this context and related strategies include constant-bearing pursuit and motion camouflage [5], [8]. Animals like bats [8] and insects [10], [11] execute pursuit with limited sensor accuracy using highly agile motion. These characteristics are especially pertinent to the bioinspired pursuit problem using small robotic vehicles.

This paper uses inspiration from the pursuit behavior of insects, in particular, male mosquitoes. We study swarming and pursuit behavior of wild mosquitoes from flight data [12]. Male mosquitoes form a mating swarm to attract a female. A female mosquito, which flies faster than the males, typically flies through the swarm several times before coupling with a single male and leaving the swarm. The mechanism that triggers male pursuit behavior is unknown, but one possibility is based on proximity [13]: once the distance to the female is sufficiently small (a close encounter), the male speeds up and pursuit starts. Fig. 1 shows trajectories of a coupling flight of male and female mosquitoes reconstructed from stereoscopic video sequences. They change their direction of motion and speed rapidly.

Manuscript received October 13, 2015; revised February 10, 2016; accepted April 8, 2016. Manuscript received in final form April 22, 2016. The work of J. K. Yim was supported by the National Science Foundation within the Division of Undergraduate Education through the Research Experiences for Undergraduate Program under Grant 1062885. Recommended by Associate Editor K. Y. Pettersen.

D. Shishika is with the Department of Aerospace Engineering, University of Maryland, College Park, MD 20742 USA (e-mail: daigo.shishika@gmail.com).

J. K. Yim is with the Department of Electrical Engineering and Computer Sciences, University of California at Berkeley, Berkeley, CA 94720 USA (e-mail: yim@eecs.berkeley.edu).

D. A. Paley is with the Department of Aerospace Engineering and the Institute for Systems Research, University of Maryland, College Park, MD 20742 USA (e-mail: dpaley@umd.edu).

Color versions of one or more of the figures in this paper are available online at http://ieeexplore.ieee.org.

Digital Object Identifier 10.1109/TCST.2016.2558538

To accommodate the aforementioned characteristics of the mosquito behavior, we consider a particle pursuit problem with nonlinear dynamics, allowing acceleration to be in an arbitrary direction. One closely related pursuit study used a sliding-mode controller [14] and another used a partial-stability-based controller [15]. We design a bioinspired pursuit law using a Lyapunov-based approach fortified by the concept of ultimate boundedness. In addition to LOS stabilization, we consider the following design criteria.

The first criterion of bioinspired pursuit is minimal control effort. In small vehicles—like in insects—the available control effort is restricted because of limited payload capacity, actuator size, and power/energy storage. Also, unlike missiles whose task ends at the target intercept, these pursuers may have to continue other tasks after intercept. Therefore, achieving target capture with low energy consumption is important.

Another criterion is robustness to uncertainties like sensor noise. The measurement errors of pertinent states like range, range rate, and LOS angular rate are often ignored in missile guidance. However, measurement error is an important consideration for a low-cost vehicle with rudimentary sensors.

The third design criterion arises in a near-miss scenario, i.e., how does the pursuer behave if the pursuit continues after a near miss? The effect of wind, losing sight of the target, or an unexpectedly fast target maneuver may cause the pursuit to fail. The near-miss scenario is also seen in mosquito coupling flight (see Fig. 1) when the distance between two mating mosquitoes becomes very small and then grows; this cycle repeats several times before they form a couple. An important strategy may be to remain close to the target after a close encounter in order to decrease the control effort for the next attempt. The same scenario also applies if the objective of the pursuer is not to intercept the target but merely to stay close to it. In this case, the pursuer may be required to continue the pursuit for a longer duration of time. This paper considers continued pursuit in the near-miss scenario, and we design the pursuit law so that it ensures robustness and efficiency.

Existing guidance laws derived with strong assumptions have proven to be useful for real missile implementation [1], but there has not been an experimental validation of a pursuit law with small agile vehicles. Experiments with heterogeneous teams of ground and aerial vehicles have been conducted for pursuit-evasion games [16]; however, our focus is on terminal guidance. We constructed an experimental testbed using custom-built autonomous hovercraft with onboard sensing and control (see Fig. 2). Hovercrafts are suitable to replicate flight conditions in two dimensions because, unlike most wheeled vehicles, they are holonomic and capable of rapid acceleration. These features make the hovercraft testbed a suitable preliminary step toward implementation of 3-D pursuit in flight.

The contributions of this paper are as follows.

1) A bioinspired pursuit law that performs well in the near-miss scenario is robust to measurement errors and has less energy consumption than existing robust pursuit laws.

Fig. 2. Left: autonomous pursuer hovercraft with onboard camera. Right: target hovercraft with IR light tower.

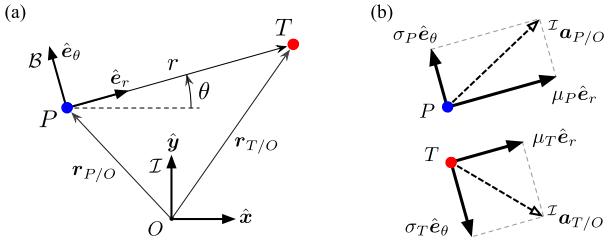

Fig. 3. (a) Definition of LOS frame $\mathcal{B}$ and the coordinate system (r, θ) where the pursuer P is pursuing the target T. (b) Decomposition of the acceleration into radial component μ and normal component σ in the LOS frame.

2) Experimental demonstration of the performance of the bioinspired pursuit law with a custom-built hovercraft testbed.
3) Analytical, numerical, and experimental comparison with existing pursuit laws.

This paper advocates replacing pursuit laws developed for missile guidance with a bioinspired algorithm designed for small agile robotic vehicles. (The bioinspired pursuit law described here was previously introduced in [17]. Detailed proofs that were omitted in [17] are included in this paper. Also, additional theoretical results considering control saturation have been added.)

This paper is organized as follows. Section II formulates the problem and introduces the basic concepts used to prove robustness. Section III introduces the basic specifications of the experimental testbed. Section IV derives the bioinspired pursuit law using Lyapunov-based control and compares it with existing pursuit laws from missile guidance. Section V presents the experimental results using the hovercraft testbed. Section VI summarizes this paper and ongoing and future work.

II. Theoretical Background

A. Problem Formulation

Consider the following formulation of the pursuit problem as a planar system of two point particles with unit mass. Let T and P denote the target and the pursuer, respectively. Fig. 3 depicts the relevant reference frames and coordinates, which includes the inertial frame $\mathcal{I} \triangleq (O, \hat{\mathbf{x}}, \hat{\mathbf{y}}, \hat{\mathbf{z}})$, the LOS frame $\mathcal{B} \triangleq (P, \hat{\mathbf{e}}_r, \hat{\mathbf{e}}_\theta, \hat{\mathbf{z}})$, the relative position vector $\mathbf{r} = \mathbf{r}_{T/O} - \mathbf{r}_{P/O}$, the range $r = \|\mathbf{r}\|$, and the LOS angle θ, where $\cos\theta = \hat{\mathbf{e}}_r \cdot \hat{\mathbf{x}}$.

The inertial kinematics of the two-particle system expressed as components in frame $\mathcal{B}$ are [18]

$$\left[\frac{^{\mathcal{I}}d^2}{dt^2}\mathbf{r}\right]_{\mathcal{B}} = \begin{bmatrix} \ddot{r} - r\dot{\theta}^2 \\ 2\dot{r}\dot{\theta} + r\ddot{\theta} \end{bmatrix}_{\mathcal{B}} = \begin{bmatrix} \mu_T - \mu_P \\ \sigma_T - \sigma_P \end{bmatrix}_{\mathcal{B}} \tag{1}$$

where μ_T and σ_T (resp. μ_P and σ_P) denote the radial and normal components of the acceleration of T (resp. P) in frame $\mathcal{B}$.

The state of the system is $\mathbf{x} = [x_1, x_2, x_3]^T \triangleq [r, \dot{r}, r\dot{\theta}]^T$. The input to the system is the relative acceleration between T and P, i.e., $\mathbf{u} = [\mu, \sigma]^T \triangleq \mathbf{u}_T - \mathbf{u}_P$, where $\mathbf{u}_T \triangleq [\mu_T, \sigma_T]^T$ and $\mathbf{u}_P \triangleq [\mu_P, \sigma_P]^T$. Noting that $x_1 > 0$, we have the following state-space system on the domain $\mathcal{D} = \mathbb{R}^+ \times \mathbb{R}^2$:

$$\begin{aligned} \dot{\mathbf{x}} &= \mathbf{f}(\mathbf{x}) + \mathbf{g}(\mathbf{x})\mathbf{u} \\ \mathbf{f}(\mathbf{x}) &= \begin{bmatrix} x_2 \\ x_3^2/x_1 \\ -x_2x_3/x_1 \end{bmatrix} \\ \mathbf{g}(\mathbf{x}) &= \begin{bmatrix} 0 & 0 \\ 1 & 0 \\ 0 & 1 \end{bmatrix}. \end{aligned} \tag{2}$$

Let δ be a small positive constant. The statement

$$\dot{r}(t) = x_2(t) < -\delta < 0 \qquad \forall\, t > T \tag{3}$$

is a sufficient condition for target intercept in finite time [14]. Having a fixed LOS-angle θ or, equivalently, satisfying the condition $x_3 = 0$, is an efficient means of target intercept [1]–[7].

We seek to design a control law $\mathbf{u}_P$ that ensures solutions of system (2) converge to the domain $\mathcal{D}_2 = \{\mathbf{x} \mid x_2 < 0, x_3 = 0\}$. In doing so, we assume the following.

- (A1) Either particle may accelerate in an arbitrary direction.
- (A2) The pursuer measures the state $\mathbf{x}$ with random errors.
- (A3) The target acceleration $\mathbf{u}_T$ is unknown, but the bound $\bar{u}_T \triangleq \max\{\|\mathbf{u}_T\|\}$ is known.
- (A4) The particles have finite size and collide only when x_1 is less than $r_0 > 0$; $x_1 = 0$ does not occur.

Assumption (A1) may not apply to typical fixed-wing aircraft or missiles since they use control surfaces to accelerate in the direction approximately normal to the body forward axis. However, (A1) is applicable to rotorcraft such as a small-scale helicopter or quadcopter, which can change its attitude quickly and accelerate in any direction.

B. Ultimate Boundedness

We introduce the following lemmas related to ultimate boundedness [19] in order to subsequently prove robustness of the pursuit law in Section IV-B.

Lemma 1: Consider a system $\dot{\mathbf{x}} = \mathbf{F}(t, \mathbf{x})$, where $\mathbf{x} \in \mathbb{R}^n$ and $\mathbf{F}(\mathbf{x})$ is piecewise continuous and locally Lipshitz in $\mathbf{x}$. Let B_e denote a simply connected set that contains a point $\mathbf{x}^*$. Let the Lyapunov function candidate be $V(\mathbf{x}) = (\mathbf{x} - \mathbf{x}^*)^T P(\mathbf{x} - \mathbf{x}^*)$, where $P > 0$. Then the solution of the system enters the set $\Omega = \left\{ \mathbf{x} \;\middle|\; V(\mathbf{x}) \le c \right\}$ in finite time T and stays there for all $t > T$ if the following conditions are true.

1) $\dot{V}(\mathbf{x}) \le -W(\mathbf{x})$ for all $\mathbf{x} \notin B_e$, where $W(\mathbf{x})$ is continuous and strictly positive in $\mathbf{x} \notin B_e$.
2) Ω contains B_e.

Proof: Suppose the solution starts at $\mathbf{x}(t_0) = \mathbf{x}_0$, and $V(\mathbf{x}_0) < c_{\max}$. Let $\Lambda = \left\{ \mathbf{x} \;\middle|\; c \le V(\mathbf{x}) \le c_{\max} \right\}$. Let $k = \min_{\mathbf{x}\in\Lambda} W(\mathbf{x}) > 0$. The minimum exists because $W(\mathbf{x})$ is continuous and Λ is compact. The solution enters Ω in finite time since

$$V(\mathbf{x}(t)) \le V(\mathbf{x}_0) - k(t - t_0) \quad \forall\, \mathbf{x} \in \Lambda$$

implies that $V(\mathbf{x}(t))$ reduces to c within the time interval $[t_0,\ t_0 + (c_{\max} - c)/k]$. The solution in Ω stays there for all future time since $\dot{V}(\mathbf{x}) < 0$ on the boundary of Ω (i.e., Ω is positively invariant). ■

Lemma 2: Using the same conditions as Lemma 1, if $W(\mathbf{x})$ [in 1) of Lemma 1] is of the form

$$W(\mathbf{x}) = (\mathbf{x} - \mathbf{x}^*)^T Q(\mathbf{x} - \mathbf{x}^*) - D$$

where $Q = \text{diag}\{\rho_1, \rho_2, \ldots, \rho_n\}$, $\rho_i > 0$, $D > 0$, and then B_e is an ellipsoidal region centered at $\mathbf{x}^*$ with axis length $\lambda_i = \sqrt{D/\rho_i}$ in each direction.

III. Experimental Testbed

The bioinspired pursuit law was implemented using a pair of small autonomous hovercrafts depicted in Fig. 2. Both hovercrafts participate in each experiment—one as pursuer and the other as target. We considered several objectives in the design of this platform: good representation of point-mass dynamics, i.e., full actuation and low drag; onboard target tracking and control; sturdiness to endure possible collisions during pursuit; and a small size to operate in the available lab space.

Conventional hovercrafts are frequently propelled by two rear-facing fans or one fan and one or more rudders to provide forward thrust and yaw torque with a small number of fans [20], [21]. However, the conventional configuration is underactuated and rotationally asymmetric, making it ill suited to our application. Other platforms add side-to-side thrusters to be fully actuated or use large numbers of thrusters, but these hovercrafts are still rotationally asymmetric [22], [23]. Stubbs *et al.* [24] developed a networked hovercraft platform that is fully actuated and rotationally symmetric; however, it uses offboard cameras for position measurements and a layout of four unidirectional thrusters for propulsion.

Each hovercraft in our testbed measures a diameter of 6.5 in and weighs between 110 and 125 g, depending on its configuration. Two lift fans carry the hovercraft, and four unidirectional thrust fans arranged as in [24] accelerate and rotate it. Each hovercraft carries an ATmega32u4 processor capable of running fully autonomous target tracking and pursuit. The pursuer tracks the target using an onboard infrared (IR) camera from a Wii-mote game controller and an MPU6050 digital 6DOF inertia measurement unit (IMU). The target hovercraft carries an IR beacon consisting of two IR light-emitting diode rings placed vertically 3 in apart. This arrangement allows the pursuer to autonomously track the target without the use of any offboard measurements.

The camera field of view is also limited to approximately 60° in azimuth. Proportional–integral–derivative control of the pursuer rotation centers the target in the camera field of view.

Target range x_1 is measured from the spacing of the IR points in the image. The range rate x_2 is calculated by differentiating the measured range with respect to time. The angle to the target from the camera axis is differentiated with respect to time to find the LOS rotation rate in the body frame. This rate is added to the body-frame rotation rate in the inertial frame as measured by the IMU to determine the LOS angular rate $\dot{\theta}$ in the inertial frame. Discrete low-pass filters are applied to all measured values in order to smooth out the discretized digital-image measurements and to reject erroneous single-measurement deviations.

Both hovercrafts are equipped with an XBee wireless transceiver with which the pursuer transmits telemetry and the evader receives wireless commands from a ground station. The ground station uses an OptiTrack motion-capture system to track the trajectories of the pursuer and evader and to control the trajectory of the evader. In addition, the ground station logs telemetry from the pursuer and matches it to motion-capture data to record the performance (e.g., sensor measurements and controller output) of the pursuer. The pursuer's onboard sensing and control system are entirely autonomous and do not require human intervention or the motion-capture system.

IV. Theoretical Results

This section presents a pursuit law designed with a Lyapunov-based approach and derives the conditions on the control gains to guarantee robust target intercept. We modify the pursuit law to accommodate noisy measurements. We also analytically and numerically compare the modified pursuit law with existing ones. Finally, we consider the effect of control saturation. The performance of the pursuit law is demonstrated by the experiments described in Section V.

A. Bioinspired Pursuit Law

One way to satisfy the target intercept condition (3) is to decrease x_2 as much as possible, as in [15]. Although this strategy may result in a short capture time, it requires a large control effort (see Section IV-D). In addition, a high closing speed may be problematic in a near-miss scenario. Another approach is to drive x_2 to a negative constant $v_{\rm cl} < 0$ representing the desired closing speed [14]. This strategy will keep x_2 at a reasonable value and eliminate the issues raised above.

Consider the positive semidefinite Lyapunov function candidate

$$\begin{aligned} V &= V_3(x_3) + V_2(x_2) \\ &= \frac{\kappa}{2}x_3^2 + \frac{1}{2}(x_2 - v_{\rm cl})^2, \quad \kappa > 0. \end{aligned} \tag{4}$$

We first find the desired relative acceleration $\mathbf{u}_{\rm des}$, and then consider the actual control law $\mathbf{u}_P$ of the pursuer.

One possible desired relative acceleration $\mathbf{u}_{\rm des}$ for the control Lyapunov function (4) was found previously using the knowledge of target acceleration and Sontag's formula [25], which is proved to have optimality in minimizing the integral of control effort and states. In contrast, we make the pursuit law robust to uncertainties like unknown target acceleration by choosing

$$\mathbf{u}_{\rm des} = \begin{bmatrix} -\dfrac{x_3^2}{x_1} - N_r(x_2 - v_{\rm cl}) \\ \left(\dfrac{x_2}{x_1} - N_\theta\right) x_3 \end{bmatrix}, \quad N_r > 0, \ N_\theta > 0. \tag{5}$$

The robustness arises from the linear terms with sufficiently large control gains N_r and N_θ (see Proposition 1). The feedback control (5) makes the derivative of the Lyapunov function V in (4) negative semidefinite along solutions of (2)

$$\dot{V} = -\kappa N_\theta x_3^2 - N_r(x_2 - v_{\rm cl})^2 \leq 0. \tag{6}$$

The quadratic terms in (6) are convenient for analyzing the robustness of the pursuit law in the sequel. Note that $\mathbf{u}_{\rm des}$ is the desired relative acceleration, whereas $\mathbf{u} = \mathbf{u}_T - \mathbf{u}_P$ is the actual relative acceleration.

If the pursuit law is chosen to be $\mathbf{u}_P = \mathbf{u}_T - \mathbf{u}_{\rm des}$, then $\mathbf{u} = \mathbf{u}_{\rm des}$ and the closed-loop system will stabilize the equilibrium point $\mathbf{x}^* = [x_2^*, x_3^*]^T = [v_{\rm cl}, 0]^T$, which ensures target capture in finite time. However, this pursuit law requires knowledge of the target acceleration $\mathbf{u}_T$. Therefore, we treat $\mathbf{u}_T$ as an external disturbance, $\mathbf{\Delta} \triangleq [\Delta_r, \Delta_\theta]^T$, and consider the pursuit law

$$\mathbf{u}_P = -\mathbf{u}_{\rm des}. \tag{7}$$

The relative acceleration achieved by (7) is

$$\mathbf{u} = \mathbf{u}_T - \mathbf{u}_P = \mathbf{u}_{\rm des} + \mathbf{\Delta} \tag{8}$$

where $\mathbf{\Delta} \equiv \mathbf{u}_T$. We consider the robustness of the controller to the disturbance $\mathbf{\Delta}$ in the next section.

Remark 1: One could use a disturbance observer [26], [27] to estimate the target acceleration and to incorporate the estimated value $\hat{\mathbf{u}}_T$ into the pursuit law, so that $\mathbf{u}_P = \hat{\mathbf{u}}_T - \mathbf{u}_{\rm des}$. However, there would still be a disturbance due to the estimation error $\mathbf{u}_T - \hat{\mathbf{u}}_T$ for a time-varying $\mathbf{u}_T$ [26], and the achieved relative acceleration would still be expressed as in (8), with $\mathbf{\Delta} \equiv \mathbf{u}_T - \hat{\mathbf{u}}_T$; the robustness analysis in the next section still applies in this case.

Remark 2: The terms $-x_3^2/x_1$ and x_2x_3/x_1 in (5) may become large when the range x_1 becomes small, although they do not grow unbounded [see Assumption (A8)]. The proposed control law avoids this issue by regulating $|x_3|$ to be small. Also, for the case where large acceleration is commanded, robustness to control saturation is considered in Section IV-E.

B. Robustness to Measurement Error

Robustness of the pursuit law to unknown target acceleration was studied in [14] using sliding-mode control and in [15] using partial-stability-based control. In those studies, signum functions were employed to address the possibility of unknown target acceleration, which was treated as a matching disturbance. However, the effect of measurement error was not considered in [14] or [15]. We show here that the proposed pursuit law (7), where $\mathbf{u}_{\rm des}$ is given by (5), is robust to both unknown target acceleration and measurement error under a proper choice of the control gains N_r and N_θ.

As observed in our experimental testbed, the measured states x_1, x_2, and x_3 typically include some amount of noise. Let the measured states (or estimated states, see Remark 1) available to the pursuer be defined as $\mathbf{x}_{\text{meas}} \triangleq \mathbf{x} + \mathbf{e}$, where $\mathbf{e} = [e_1,\ e_2,\ e_3]^T$ denotes the measurement (or estimation) error. We make the following additional assumptions regarding the error based on the experimental testbed.

(A5) The error on the range measurement e_1 may be ignored, since it is sufficiently small compared with e_2 and e_3.

(A6) $|e_i| \ll |x_i|$ for $i = 1, 2, 3$, so the error terms that are higher than first order may be ignored.

(A7) The magnitudes $|e_2|$ and $|e_3|$ are bounded by constants e_2^* and e_3^*, respectively, where $e_2^* < |v_{\text{cl}}|$ and $e_3^* < |v_{\text{cl}}|/\sqrt{\kappa}$.

The validity of these assumptions for the experimental testbed is discussed in Section V. Since the upper bound on the vehicle speed (which limits x_3) and the lower bound on the range (x_1) both exist in the physical implementation, we also assume the following.

(A8) The absolute value of the LOS rate $|\dot{\theta}| = |x_3/x_1|$ is bounded by a constant, $\omega > 0$.

The desired acceleration term $\mathbf{u}_{\text{des}}$ in (7) is implemented with the measured states $\mathbf{x}_{\text{meas}}$, and the input $\mathbf{u}$ in (8) becomes

$$\begin{aligned}\mathbf{u} &= \mathbf{u}_{\text{des}}(\mathbf{x}_{\text{meas}}) + \Delta \\ &= \begin{bmatrix} -\dfrac{(x_3+e_3)^2}{x_1+e_1} - N_r(x_2+e_2-v_{\text{cl}}) + \Delta_r \\ \left(\dfrac{x_2+e_2}{x_1+e_1} - N_\theta\right)(x_3+e_3) + \Delta_\theta \end{bmatrix}.\end{aligned}$$

Let $\tilde{x}_2 \triangleq x_2 - v_{\text{cl}}$. The derivative of the Lyapunov function candidate in (6) becomes

$$\dot{V} = \dot{V}_2 + \dot{V}_3$$

where

$$\dot{V}_2 = -N_r\tilde{x}_2^2 - N_r\tilde{x}_2 e_2 - 2\frac{x_3}{x_1}\tilde{x}_2 e_3 + \tilde{x}_2\Delta_r$$

and

$$\dot{V}_3 = \kappa\left(-N_\theta x_3^2 - N_\theta x_3 e_3 + \frac{x_3}{x_1}(x_3 e_2 + x_2 e_3) + x_3\Delta_\theta\right).$$

Proposition 1: The pursuit law (7) is robust to disturbance $\mathbf{\Delta}$ and measurement error $\mathbf{e}$ if the control gains are chosen to satisfy

$$N_r > \frac{\bar{u}_T + 2\omega e_3^*}{|v_{\text{cl}}| - e_2^*} \tag{9}$$

and

$$N_\theta > \frac{\sqrt{\kappa}(2\bar{u}_T + 2\omega e_2^* + \omega e_3^* + 4\kappa\omega e_3^*)}{2|v_{\text{cl}}| - 2\sqrt{\kappa}e_3^*}. \tag{10}$$

Moreover, if $\mathbf{e}$ is ignored, conditions (9) and (10) simplify to

$$N_r > \frac{\bar{u}_T}{|v_{\text{cl}}|} \quad \text{and} \quad N_\theta > \frac{\sqrt{\kappa}\bar{u}_T}{|v_{\text{cl}}|}. \tag{11}$$

Proof: Since the worst case of $\dot{V}_2$ can be decoupled from the x_3 dynamics by Assumption (A8), we first show that x_2 is bounded in steady state using the Lyapunov function $V_2(x_2)$.

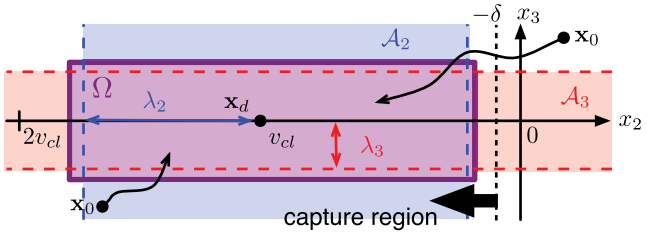

Fig. 4. Ultimate boundedness of the solutions in the x_2x_3 plane. The solutions starting at any initial condition $\mathbf{x}_0$ are guaranteed to converge to regions $\mathcal{A}_2$ and $\mathcal{A}_3$. Convergence to the set Ω lying on the left side of $x_2 = -\delta$ ensures target capture in finite time.

The cross terms, for example, $\tilde{x}_2 e_2$, may be bounded by $|\tilde{x}_2 e_2| \le (1/2)(c_1\tilde{x}_2^2 + e_2^2/c_1)$ using a constant $c_1 > 0$. Bounding the other cross terms using positive constants c_i, $i = 2, 3$, and using (A5), (A6), and (A8) yields

$$\begin{aligned}\dot{V}_2 \le\ & -N_r\tilde{x}_2^2 + \frac{N_r}{2}\left(c_1\tilde{x}_2^2 + \frac{e_2^{*2}}{c_1}\right) \\ & + \omega\left(c_2\tilde{x}_2^2 + \frac{e_3^{*2}}{c_2}\right) + \frac{1}{2}\left(c_3\tilde{x}_2^2 + \frac{\bar{u}_T^2}{c_3}\right).\end{aligned}$$

Choosing the constants to be

$$c_1 = \frac{e_2^*}{|v_{\text{cl}}|},\quad c_2 = \frac{e_3^*}{|v_{\text{cl}}|},\quad \text{and}\quad c_3 = \frac{\bar{u}_T}{|v_{\text{cl}}|}$$

we have

$$\dot{V}_2 \le -\rho_2(x_2 - v_{\text{cl}})^2 + D_2$$

where

$$\rho_2 = \left(1 - \frac{e_2^*}{2|v_{\text{cl}}|}\right)N_r - \frac{\bar{u}_T + 2\omega e_3^*}{2|v_{\text{cl}}|}$$

and

$$D_2 = \frac{|v_{\text{cl}}|}{2}(\bar{u}_T + N_r e_2^* + 2\omega e_3^*).$$

Lemmas 1 and 2 apply if $\rho_2 > 0$, which is true when N_r satisfies condition (9). From Lemmas 1 and 2, the solutions of the system converge to a region $\mathcal{A}_2 = \{\mathbf{x} \mid x_2 \in \Omega_2\}$, where Ω_2 is a line segment that contains the set $B_2 \triangleq \{|x_2 - v_{\text{cl}}| \le \lambda_2 = \sqrt{D_2/\rho_2}\}$, which is a 1-D analog of the ellipsoidal region in Lemma 2.

One may choose λ_2 to be small so that x_2 converges to a small region around v_{cl}. However, in order to require less control effort, we seek to relax as much as possible the requirements on the control gain N_r. Making use of condition (3), it is sufficient for solutions to fall inside the set Ω_2 lying in the left-half plane in Fig. 4 (strictly speaking, to the left of the line $x_2 = -\delta$). A suitable $\delta > 0$ and Ω_2 exist if $\lambda_2 < |v_{\text{cl}}|$, which is equivalent to $D_2 < |v_{\text{cl}}|^2\rho_2$. Using the expressions for D_2 and ρ_2 above, the latter condition reduces to (9).

Suppose condition (9) is satisfied, then there exist $T \ge 0$ such that $x_2 \in \Omega_2, \forall\, t > T$. After entering Ω_2, x_2 is bounded as $0 < x_2^2 < 4v_{\text{cl}}^2$. Although $\dot{V}_3$ includes the x_2^2 term, we use this inequality and positive constants c_i, $i = 4, 5, 6, 7$, to

bound $\dot{V}_3$ as

$$\frac{\dot{V}_3}{\kappa} \le -N_\theta x_3^2 + \frac{N_\theta}{2}\left(c_4 x_3^2 + \frac{e_3^{*2}}{c_4}\right) + \frac{1}{2}\left(c_7 x_3^2 + \frac{\bar{u}_T^2}{c_7}\right) + \frac{\omega}{2}\left(4c_5 v_{\rm cl}^2 + \frac{e_3^{*2}}{c_5} + c_6 x_3^2 + \frac{e_2^{*2}}{c_6}\right).$$

Note that the above inequality is valid for $t > T$. Choosing the constants to be

$$c_4 = c_5 = \frac{\sqrt{\kappa} e_3^*}{|v_{\rm cl}|}, \quad c_6 = \frac{\sqrt{\kappa} e_2^*}{|v_{\rm cl}|}, \quad \text{and} \quad c_7 = \frac{\sqrt{\kappa}\bar{u}_T}{|v_{\rm cl}|}$$

we have

$$\dot{V}_3 \le -\kappa\rho_3 x_3^2 + \kappa D_3$$

where

$$\rho_3 = \left(1 - \frac{\sqrt{\kappa} e_3^*}{2|v_{\rm cl}|}\right) N_\theta - \frac{\sqrt{\kappa}(\bar{u}_T + \omega e_2^*)}{2|v_{\rm cl}|}$$

and

$$D_3 = \frac{|v_{\rm cl}|}{2\sqrt{\kappa}}(\bar{u}_T + N_\theta e_3^* + \omega e_2^* + \omega e_3^* + 4\kappa\omega e_3^*).$$

The condition $\rho_3 > 0$ is true if N_θ satisfies condition (10). By the same argument as above, we seek the condition for the convergence of the solutions to $\mathcal{A}_3 = \{\mathbf{x} \mid x_3 \in \Omega_3\}$, where the set Ω_3 contains $B_3 \triangleq \{|x_3| \le \lambda_3 = \sqrt{D_3/\rho_3}\}$.

Consider the condition $\lambda_3 < |v_{\rm cl}|/\sqrt{\kappa}$, which is equivalent to $\kappa D_3 < |v_{\rm cl}|^2\rho_3$. Using the expressions for D_3 and ρ_3 above, this condition reduces to (10). A large κ stabilizes x_3 to a small value while requiring greater control effort [see (10)]. Nonetheless, the solution is guaranteed to converge to the rectangular region $\Omega \triangleq \{\mathbf{x} \mid x_2 \in \Omega_2,\ x_3 \in \Omega_3\}$ in Fig. 4, which completes the proof. ■

C. Modification of the Pursuit Law

Although convergence to a rectangular region provides a relaxed condition on the control gains, the required control may be large if the terms $|x_2 - v_{\rm cl}|$ or $|x_3|$ are initially large. This problem is not restricted to the initial conditions; for example, if the measurement error is large, it may cause an erroneously large control input.

In order to avoid this issue and to keep the acceleration command small even in the presence of measurement error, we saturate the linear terms in (5) using the saturation function

$$\text{sat}(x) = \begin{cases} x, & \text{if } |x| \le 1 \\ 1, & \text{otherwise.} \end{cases}$$

The saturated control is

$$\mathbf{u}_{\rm des} = \begin{bmatrix} -\dfrac{x_3^2}{x_1} - N_r' \text{sat}\left(\dfrac{x_2}{|v_{\rm cl}|} + 1\right) \\ \dfrac{x_2 x_3}{x_1} - N_\theta' \text{sat}\left(\dfrac{\sqrt{\kappa}}{|v_{\rm cl}|} x_3\right) \end{bmatrix} \tag{12}$$

where $N_r' = N_r|v_{\rm cl}|$ and $N_\theta' = N_\theta|v_{\rm cl}|/\sqrt{\kappa}$. Note that the saturated terms are identical to the original terms when $|\tilde{x}_2| \le |v_{\rm cl}|$ and $|x_3| \le |v_{\rm cl}|/\sqrt{\kappa}$. The nonlinear terms are excluded from the saturation function in order to ensure cancelation of $\mathbf{f}(\mathbf{x})$ in (2). Note that the ultimate boundedness property still holds after this modification, which is proved as follows.

It is sufficient to show that $\dot{V}_2$ and $\dot{V}_3$ are still negative in the region where the linear terms are actually saturated. For the radial component V_2, the saturated control (12) yields

$$\begin{aligned} \dot{V}_2 &= \tilde{x}_2\dot{x}_2 \\ &= \tilde{x}_2\left(\frac{x_3^2}{x_1} - \frac{(x_3 + e_3)^2}{x_1 + e_1} - N_r'\text{sgn}(\tilde{x}_2) + \Delta_r\right) \\ &< \tilde{x}_2\text{sgn}(\tilde{x}_2)(2\omega e_3^* - N_r' + \bar{u}_T) \\ &= -|\tilde{x}_2|\left(N_r' - 2\omega e_3^* - \bar{u}_T\right). \end{aligned}$$

Noting that $N_r' \triangleq N_r|v_{\rm cl}| > 2\omega e_3^* + \bar{u}_T$ [if we choose N_r according to (9)], the term inside the parentheses is positive, and we have $\dot{V}_2 < 0$. The stability of the normal component V_3 can be proved in a similar way.

D. Comparison With Other Pursuit Laws

In order to distinguish (7) from other pursuit laws, let $\mathbf{u}_A$ denote pursuit law (7), where $\mathbf{u}_{\rm des}$ is given by (12). We compare $\mathbf{u}_A$ with the partial-stability-based controller [15], $\mathbf{u}_B$, and with the sliding-mode controller [14], $\mathbf{u}_C$, which are also robust to unknown target acceleration; $\mathbf{u}_B$ and $\mathbf{u}_C$ are

$$\mathbf{u}_B = \begin{bmatrix} \mu_B \\ \sigma_B \end{bmatrix} = \begin{bmatrix} \dfrac{x_3^2}{x_1} - \nu x_2 + \eta_1 \\ \left(-\dfrac{x_2}{x_1} + N\right) x_3 + \eta_2 \text{sat}\left(\dfrac{x_3}{\varepsilon}\right) \end{bmatrix} \tag{13}$$

and

$$\mathbf{u}_C = \begin{bmatrix} \mu_C \\ \sigma_C \end{bmatrix} = \begin{bmatrix} \dfrac{x_3^2}{x_1} + \eta_1 \text{sat}\left(\dfrac{x_2 - v_{\rm cl}}{\varepsilon}\right) \\ -(N+1)\dfrac{x_2 x_3}{x_1} + \eta_2 \text{sat}\left(\dfrac{x_3}{\varepsilon}\right) \end{bmatrix} \tag{14}$$

where $\nu, N, \varepsilon > 0$, $\eta_1 > \bar{u}_T$, and $\eta_2 > \bar{u}_T$. Also consider a naive controller, $\mathbf{u}_D$, whose radial acceleration is constant, i.e., $\mu_D = \mu^*$, and whose normal acceleration is $\sigma_D = \sigma_A$.

Remark 3: The pursuit law μ_B requires $x_2(0) < 0$ for an initial condition [15], whereas law μ_A and the sliding-mode control μ_C are robust to $x_2(0) > 0$.

Metrics often used in comparing pursuit strategies include the capture time, the required σ_P, and the required μ_P. There is no significant difference in the performance and control effort in the normal component between the considered pursuit laws, as can be seen in [15] and also in the numerical simulations shown below. Once $\dot{\theta} \approx 0$, short capture times are achieved using a large μ_P, which can be seen from the dynamics (2), i.e., $\dot{x}_2 = \mu_T - \mu_P$ when $x_3 = 0$. Therefore, to achieve a pursuit law with a short capture time, one needs simply to command the maximum available radial acceleration. Based on these observations, we focus on the radial component and compare the control effort and energy consumption required for robust target capture.

Since all of the pursuit laws except $\mathbf{u}_D$ have the term x_3^2/x_1, which cancels the centrifugal acceleration in $\mathcal{B}$, let

$$G \triangleq \mu - \frac{x_3^2}{x_1} \tag{15}$$

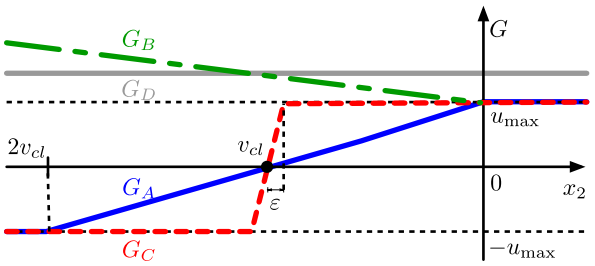

Fig. 5. Comparison of the controller specific terms G [see (15)] in the radial control as a function of range rate x_2. For simplicity, $x_3 = 0$ is assumed for the naive controller G_D. The pursuit law G_A has the smallest absolute value, which results in the smallest control effort.

denote the additional term on the radial component, and compare G from the three pursuit laws. For a fair comparison, we choose the smallest control gains for N_r and η_1 that guarantee robustness (strictly speaking, the limiting value, i.e., if $N > a$ is required, then we choose $N = a$). Small constants ν and ε are retained as parameters. Only the no-measurement-error case is considered since measurement error was not studied in [14] and [15].

From conditions (11) and (12), $N'_\theta = \bar{u}_T$. The additional terms G of the control laws with minimal gains are

$$
\begin{aligned}
G_A &= \bar{u}_T \,\mathrm{sat}\left(\frac{x_2}{|v_{\mathrm{cl}}|} + 1\right) \\
G_B &= -\nu x_2 + \bar{u}_T \\
G_C &= \bar{u}_T \,\mathrm{sat}\left(\frac{x_2 - v_{\mathrm{cl}}}{\varepsilon}\right) \\
G_D &= \mu^* - x_3^2/x_1.
\end{aligned}
$$

Fig. 5 shows G as a function of x_2. Noting that $\mathbf{u}_A$ ensures $\tilde{x}_2 < |v_{\mathrm{cl}}| \Leftrightarrow 2v_{\mathrm{cl}} < x_2 < 0$ after a certain amount of time, G_A has the smallest absolute value for the same states $\mathbf{x}$.

Remark 4: The sliding-mode controller μ_C becomes identical to μ_A if $\varepsilon = |v_{\mathrm{cl}}|$. Although ε is typically a small value introduced in order to avoid the chattering from the signum function [14], it may be as large as $|v_{\mathrm{cl}}|$ and still guarantees robustness. In the particular case for which the smallest control gains are considered, the proposed controller μ_A can be categorized as a sliding-mode controller with sliding surface relaxed as much as possible while maintaining robustness. The comparative study shows the advantage of this design philosophy with respect to the design criteria that we consider.

Fig. 6 shows the results of numerical simulations up to the time of the first close encounter. The open-loop trajectory of the target is specified by $\mathbf{u}_T(t) = [0.5\sin(0.4\pi t + 0.3\pi), 0.5\sin(\pi t + 0.4\pi)]$, and the initial conditions are $\mathbf{r}_{P/O}(0) = [0, 0]$, $\mathbf{v}_{P/O}(0) = [0, 0]$, $\mathbf{r}_{T/O}(0) = [2, 0]$, and $\mathbf{v}_{T/O}(0) = [-0.5, 0.7]$. Parameters and control gains were $v_{\mathrm{cl}} = -2.0$, $\kappa = 400$, $\nu = 0.1$, $N = 2$, $\varepsilon = 0.1$, and $\bar{u}_T = 0.5$, which gives $N'_r = N'_\theta = \eta_1 = \eta_2 = 0.5$. The naive control law $\mathbf{u}_D$ is simulated with $\mu_1^* = 0.4$ and $\mu_2^* = 0.7$, denoted by Naive 1 and Naive 2, respectively. Define the energy consumption as $E_{tot} = \int_{t_0}^{t} \|\mathbf{u}(\tau)\|^2 \, d\tau$ [28]. Since the motor voltage is proportional to the magnitude of the acceleration command, E_{tot} is proportional to the amount of energy consumption,

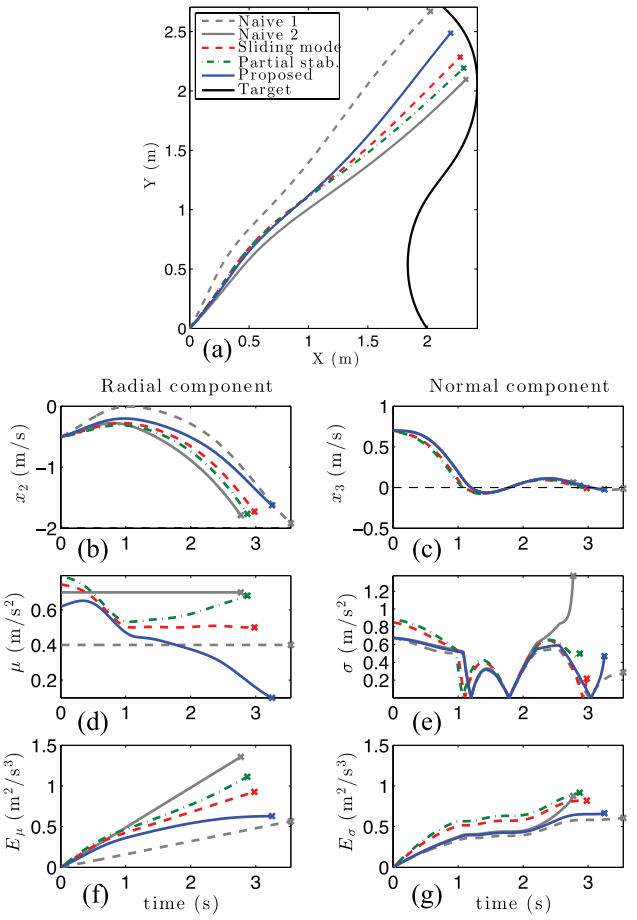

Fig. 6. Numerical simulation until the first close encounter. (a) Trajectories from different pursuit laws against the same target (black solid line). (b) and (c) States. (d) and (e) Absolute value of acceleration commands. (f) and (g) Energy expenditure calculated from the time integral of squared acceleration commands. The left and right columns describe the radial and normal components in the LOS frame, respectively.

assuming that the motor impedance is approximately constant. E_μ and E_σ are the radial and normal components of the energy consumption. Comparison of the normal component differs only at the end, when x_1 becomes small. In the radial component, the bioinspired control law (blue solid line) has the smallest maximum acceleration and energy consumption.

Fig. 7 shows the case when the pursuit is continued after the first close encounter. This scenario corresponds to a near miss or target tracking. To quantify the performance, look at the energetic cost $J = \int_0^t \{x_1(\tau)\}^2 d\tau$ shown in Fig. 7(b). The bio-inspired pursuit law has the smallest J and the smallest energy consumption E_{tot}. Fig. 7(d) shows a phase portrait in x_2x_3 space. At the instant of a near miss, the range rate x_2 changes sign from negative to positive, but the solution returns to the set Ω (see the proof of Proposition 1) in finite time.

E. Robustness to Control Saturation

In the pursuit problem considered thus far, as well as in [14] and [15], the pursuer may achieve arbitrary acceleration, i.e., it can accelerate in any direction with any magnitude. Under such an assumption, the pursuit law (7)

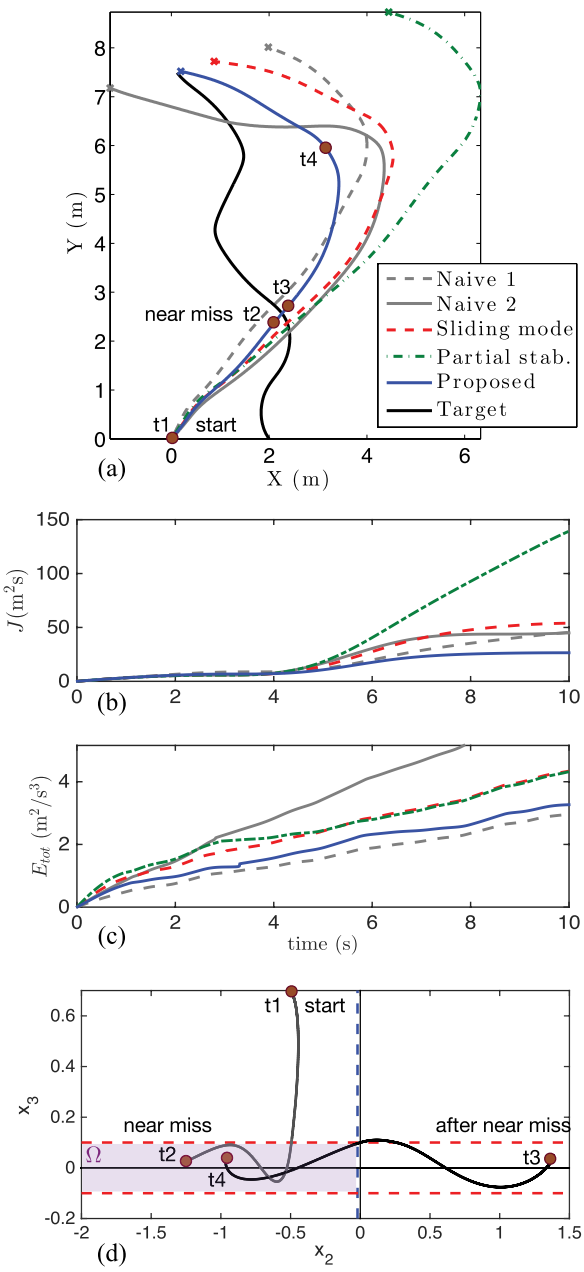

Fig. 7. Numerical simulation of near-miss scenario. (a) Trajectories from different pursuit laws against the same target (black solid line). (b) Energetic cost, which penalizes the deviation from the target. (c) Total energy expenditure E_{tot}. (d) Phase portrait in x_2x_3 space for the proposed controller. The time stamps $t1$–$t4$ correspond to those in (a).

effectively cancels the vector field $\mathbf{f}(\mathbf{x})$ in (2) and adds a vector field $[-N_r\tilde{x}_2, -N_\theta x_3]^T$ that is sufficiently strong to drive the solution of the system to $\mathbf{x}^*$, even in the presence of uncertainty $\mathbf{\Delta}$. However, the cancelation of $\mathbf{f}(\mathbf{x})$ is not always possible, e.g., in a physical implementation for which the acceleration is limited. This section considers the robustness of the pursuit law to control saturation.

To simplify the analysis, consider $\mathbf{u}_{\text{des}}$ in (5) without the measurement errors, and the case where the target is under a naive evasive maneuver

$$\mathbf{u}_T = \begin{bmatrix} \mu_T \\ \sigma_T \end{bmatrix} = \begin{bmatrix} \bar{u}_T \\ \bar{u}_T \text{sign}(x_3) \end{bmatrix}. \tag{16}$$

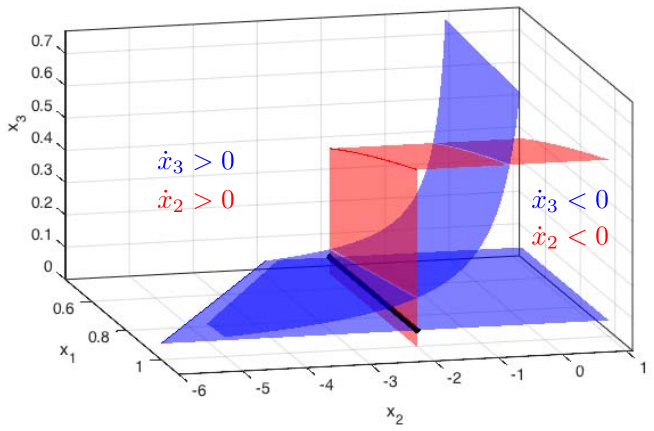

Fig. 8. Nullclines of the system, i.e., surfaces where $\dot{x}_2 = 0$ (red region) and $\dot{x}_3 = 0$ (blue region). The surface for $\dot{x}_1 = 0$, which is an x_1x_3 plane at $x_2 = 0$, is omitted for clarity.

This evasive strategy increases the range rate by accelerating away from the pursuer and increasing the LOS rate. The target tries to avoid what the pursuer is trying to achieve—zero LOS rate and negative range rate.

Let $\bar{u}_P$ denote the bound on pursuer's acceleration in each direction, i.e., $\eta_P, \sigma_P \leq \bar{u}_P$. With the pursuit strategy (7) and evasive strategy (16), system (2) is described as

$$\dot{\mathbf{x}} = \begin{bmatrix} x_2 \\ x_3^2/x_1 - \bar{u}_P \text{sat}\left(\dfrac{h_1(\mathbf{x})}{\bar{u}_P}\right) + \bar{u}_T \\ -x_2x_3/x_1 - \bar{u}_P \text{sat}\left(\dfrac{h_2(\mathbf{x})}{\bar{u}_P}\right) + \bar{u}_T \text{sign}(x_3) \end{bmatrix}$$

where

$$\begin{bmatrix} h_1(\mathbf{x}) \\ h_2(\mathbf{x}) \end{bmatrix} = \begin{bmatrix} x_3^2/x_1 + N_r(x_2 - v_{\text{cl}}) \\ -x_2x_3/x_1 + N_\theta x_3 \end{bmatrix}.$$

Let $\bar{u} \triangleq \bar{u}_P - \bar{u}_T > 0$. Also, let N_r^* and N_θ^* denote the limiting gain values that satisfy (11), i.e., $N_r^* \triangleq \bar{u}_T/|v_{\text{cl}}|$ and $N_\theta^* \triangleq \sqrt{\kappa}\bar{u}_T/|v_{\text{cl}}|$.

Proposition 2: The pursuit law (7) is robust to control saturation and evasive maneuver (16) if $\bar{u} = \bar{u}_P - \bar{u}_T > 0$ and the control gains satisfy condition (11) and

$$\frac{N_\theta^*}{N_\theta}\left(1 - \frac{N_r^*}{N_r}\right)\sqrt{\kappa} < 1 \tag{17}$$

with $\sqrt{\kappa} = |v_{\text{cl}}|/\sqrt{\bar{u}r_0}$.

Proof: Fig. 8 shows the nullclines of the system with the proper choice of control gains. By symmetry, consider only the positive x_3 region ($x_3 = 0$ is a separatrix). From the sign of $\dot{x}_2$ and $\dot{x}_3$ in each area separated by the nullclines, observe that the black solid line is a stable manifold. Hence, the following two conditions guarantee target capture: 1) the stable manifold exists and lies in the negative x_2 region and 2) the stable manifold intersects the surface $x_1 = r_0$.

We express these conditions in a different way by looking at the 2-D slice of the nullclines for each x_1 value. Fig. 9 shows four configurations of the nullclines arising from different choices of the control gains and x_1. The locations of the solid lines are determined by the system parameters $\bar{u}$ and r_0,

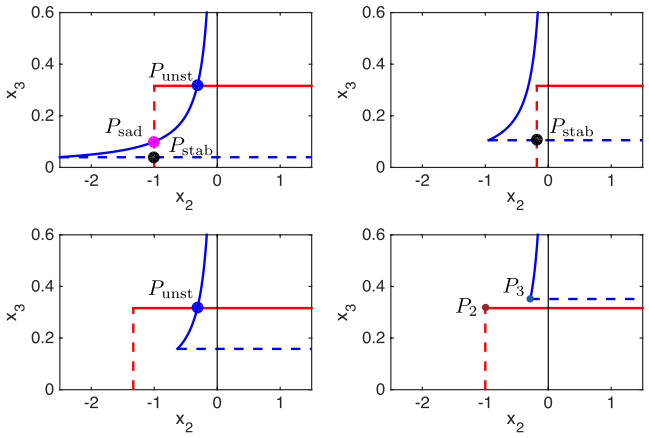

Fig. 9. Four different configurations of nullclines. The red and blue lines correspond to nullclines for $\dot{x}_2$ and $\dot{x}_3$, respectively. P_{stab}, P_{unst}, and P_{sad} denote stable node, unstable node, and saddle point, respectively.

whereas the dashed lines are determined by the control gains v_{cl}, κ, N_r, and N_θ (chosen by the pursuer). The intersecting points of the dashed and solid lines are denoted by P_2 and P_3, respectively (right bottom in Fig. 9).

The top two configurations in Fig. 9 have a stable manifold, but the bottom two do not. The stable manifold exists if and only if point P_2 is above and to the right of point P_3. Also, the stable node has to be in the negative x_2 region in order to ensure target capture. The coordinates of those points are $P_2 = [v_{\text{cl}} + \bar{u}_T/N_r, \sqrt{\bar{u}x_1}]$, $P_3 = [-N_\theta x_1 \bar{u}/\bar{u}_T, \bar{u}_T/N_\theta]$, and $P_{\text{stab}} = [v_{\text{cl}} + \bar{u}_T/N_r, \bar{u}_T/N_\theta]$, assuming $\bar{u} \triangleq \bar{u}_P - \bar{u}_T > 0$.

Hence, the stability conditions required at each x_1 are as follows.

1) The stable node must lie to the left of $x_2 = 0$

$$v_{\text{cl}} + \frac{\bar{u}_T}{N_r} < 0. \tag{18}$$

2) P_2 must be above P_3

$$\frac{\bar{u}_T}{N_\theta} < \sqrt{\bar{u}x_1}. \tag{19}$$

3) P_2 must be on the right side of P_3

$$-N_\theta x_1 \frac{\bar{u}}{\bar{u}_T} < v_{\text{cl}} + \frac{\bar{u}_T}{N_r}. \tag{20}$$

Since conditions 2) and 3) become more stringent for smaller x_1, the conditions are satisfied for all $x_1 > r_0$ if they are satisfied at $x_1 = r_0$. By choosing the parameter κ as $\kappa = |v_{\text{cl}}|^2/\bar{u}r_0$, the three conditions at $x_1 = r_0$ are rewritten as follows.

1) $N_r^* < N_r$.
2) $N_\theta^* < N_\theta$.
3) $\frac{N_\theta^*}{N_\theta}\left(1 - \frac{N_r^*}{N_r}\right)\sqrt{\kappa} < 1$.

Note the first two conditions 1) and 2) are equivalent to condition (11). ■

Because control gains that satisfy (17) always exist, Proposition 2 ensures that the pursuit law is robust to control saturation as long as the pursuer has maximum acceleration larger than the naive evader. Although we treated the effects of measurement error and control saturation separately in this section, the experimental results presented in the following section demonstrate the robustness of the pursuit law to the combination of measurement error, unknown target maneuvers, and control saturation.

TABLE I
CHARACTERISTICS OF THE STATE MEASUREMENT ERRORS

	Units	Mean	S.D.	Max.
e_1	m	0.023	0.031	0.14
e_2	m/s	0.112	0.289	2.26
e_3	m/s	-0.002	0.151	3.15

V. EXPERIMENTAL RESULTS

The various pursuit laws described above were implemented using the autonomous hovercraft testbed. A motion-capture camera system was employed to position the vehicles to the desired initial conditions in the inertial frame, to command a repeatable trajectory for the target, and to analyze the pursuit performance by measuring the ground truth. Initial conditions and target trajectory identical to the numerical simulation were used.

A. Measurement Noise

Vision-based tracking like that used on the pursuer hovercraft is a low-power light-weight tracking solution for a small payload-limited platform. Measurements of the range and body-frame angle to the target from the pursuer are corrupted by limited camera resolution, occasional extraneous IR sources and reflections, and other random noise. Differentiation of this noisy signal to calculate the radial and angular velocities further exacerbates the high-frequency noise. Table I shows the measurement errors across eighteen pursuit trials.

Fig. 10(a) shows an example of the measured states that are corrupted with noise. Due to the generally large size of e_2 and e_3 and infrequent extreme deviations in e_3, e_i often approaches x_i and even occasionally exceeds it, though the error-to-signal ratio is usually less than 0.5, as shown in Fig. 10(b). Hence, Assumption (A6) is marginally true for e_2 and e_3. With the controller parameters $v_{\text{cl}} = -2$ and $\kappa = 10$, the magnitudes of e_2 and e_3 agree with Assumption (A7) most of the time; $|e_2| > |v_{\text{cl}}|$ and $|e_3| > |v_{\text{cl}}|/\sqrt{\kappa}$ occur only 0.42% and 0.73% of the time. We estimate the bounds as $e_2^* = 0.56$ m/s and $e_3^* = 0.30$ m/s using two standard deviations, which accommodate 97.6% and 95.4% of all errors. Assumption (A8) is reasonable since the upper bound on the vehicle speed (which limits x_3) and the lower bound on the range both exist in the hardware implementation. We estimate the maximum LOS angular rate as $\omega = 1$ rad/s.

The control gains calculated from (9), (10), and (12) are $N_r' = 1.1$ and $N_\theta' = 12.4$; $N_r' = N_\theta' = 0.5$ from (11) when the measurement error is ignored. Although the mean capture time from ten experimental trials increased from 2.7 s with the former control gains to 3.2 s with the latter control gains, robust target capture was still achieved with the smaller gain setting, which implies that the condition to ensure robustness to measurement error may be conservative for this testbed.

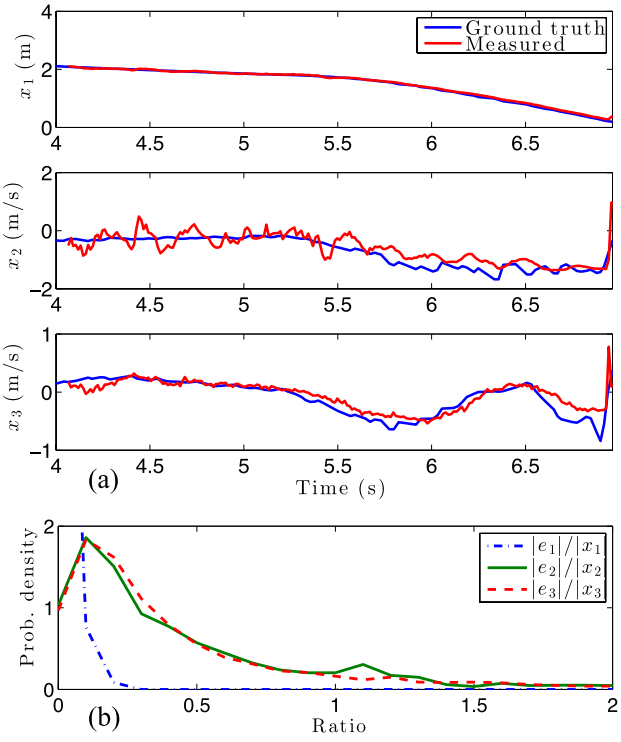

Fig. 10. (a) Example of measured states corrupted with noise. (b) Probability density of error-to-signal ratio from 18 trials.

B. Comparison Between Pursuit Laws

As in the numerical simulations, we ran each controller against a preprogrammed target trajectory and recorded the pursuer's trajectory, onboard state measurements, and control effort. The parameters and control gains were identical to those in the numerical simulations. Fig. 11 shows the results from conducting identical experimental trials for each law. Note that μ and σ in Fig. 11(d) and (e) are not the acceleration commands from the control law but those values after saturation at 1 m/s^2 due to the limitation of the motor. We characterize controller performances by capture time, maximum control command, and energy expenditure. As in Section IV, we are most interested in the maximum control command and energy expenditure since both the control authority and energy capacity are particularly limited on small vehicles. Each controller was run three times, and the average of each of the above metrics is listed in Table II. The symbols $\mu_{\max}$, $U_{\max}$, E_μ, E_{tot}, and T_{cap} denote maximum commanded radial acceleration, maximum commanded total acceleration, radial energy expenditure, total energy expenditure, and capture time, respectively. The bio-inspired controller has the smallest acceleration, the smallest energy expenditures, and the longest capture time. The naive pursuit law has the shortest capture time and the largest energy expenditure.

C. Comparison With Theory

Our experimental pursuit implementation revealed several insights compared with analytical and numerically simulated results. First, the experiments provide a realistic baseline for noise in small low-cost vision-based sensors used in pursuit.

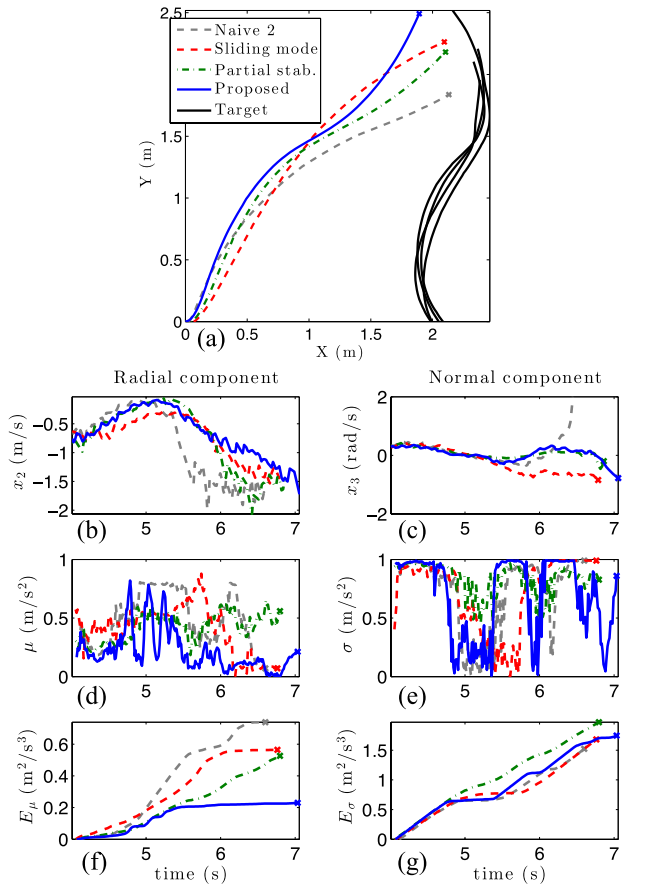

Fig. 11. Experimental trial up until the first close encounter. (a) Trajectories from different pursuit laws against the same target (black solid line). (b) and (c) States. (d) and (e) Absolute value of acceleration commands. (f) and (g) Energy expenditure calculated from the time integral of squared acceleration commands. The left and right columns describe the radial and normal components in the LOS frame, respectively.

TABLE II
PERFORMANCE OF VARIOUS PURSUIT LAWS

	$\mu_{\max}$ (m/s^2)	$U_{\max}$ (m/s^2)	E_μ (m^2/s^3)	E_{tot} (m^2/s^3)	T_{cap} (s)
Proposed	0.81	3.70	0.30	1.80	3.16
Partial stab.	1.18	5.46	0.53	2.48	2.90
Sliding mode	1.13	6.63	0.68	2.02	2.88
Naive	0.80	6.70	0.79	2.38	2.75

As expected, differentiated rate measurements like x_2 and x_3 are significantly noisier than direct range or angle measurements, like x_1, when using vision sensors such as the camera on the pursuer. Though the magnitude of the noise in x_2 and x_3 violated the theoretical assumptions, the controllers' success demonstrates that a well-designed controller may still reliably achieve target capture outside of the guaranteed operating regime.

Second, actuator saturation due to limited actuator authority changed controller performance compared with simulation, emphasizing the importance of a low maximum commanded acceleration. Since no bound is assumed on pursuer acceleration in the controller derivations, unachievable acceleration magnitudes might be commanded. This problem

is exacerbated by sensor noise, which may produce erroneously large state measurements and corresponding large fluctuations in acceleration commands. In the experimental implementation, overly large acceleration commands are saturated by scaling down to the maximum achievable acceleration magnitude while maintaining the original direction. In particular, saturation modified the achieved acceleration when either μ or σ exceeded the maximum acceleration magnitude. This effect is observed in the experimental σ acceleration, in which the controllers differ from each other earlier in pursuit than they do in simulation. The effects of actuator limits may be avoided or mitigated by limiting the maximum commanded acceleration or by different scaling and saturating strategies when unachievable accelerations are commanded.

VI. Conclusion

Inspired by the pursuit behavior of flying insects, we consider low-energy consumption, robustness to uncertainty, and performance in the near-miss scenario to design a bio-inspired pursuit law for small agile robotic vehicles using Lyapunov-based control. We performed analytical, numerical, and experimental comparison of various pursuit laws and showed that the bio-inspired law has the least energy consumption—while staying closest to the target in a near-miss scenario—among all those considered, including a sliding-mode controller and a partial-stability-based controller.

Experiments showed that the magnitude of the measurement error was not negligible. Lyapunov analysis together with the concept of ultimate boundedness established the robustness of the bio-inspired pursuit law to unknown target acceleration and measurement error. Experiments also showed that the gain condition for robustness is conservative, which may have been caused by deterministic analysis of the error bounds. In ongoing work, we are considering 3-D pursuit and a stochastic approach to model the effect of measurement error.

Acknowledgment

The authors would like to thank J. Fiene for providing cameras used in the hovercraft. The authors would also like to thank D. Yeo and F. Lagor for the valuable discussions.

References

[1] P. Zarchan, *Tactical and Strategic Missile Guidance* (Progress in Astronautics and Aeronautics), vol. 176. Washington, DC, USA: American Institute of Aeronautics and Astronautics, 2002.

[2] F. W. Nesline and P. Zarchan, "A new look at classical vs modern homing missile guidance," *J. Guid., Control, Dyn.*, vol. 4, no. 1, pp. 78–85, 1981.

[3] S. N. Ghawghawe and D. Ghose, "Pure proportional navigation against time-varying target manoeuvres," *IEEE Trans. Aerosp. Electron. Syst.*, vol. 32, no. 4, pp. 1336–1347, Oct. 1996.

[4] F. P. Adler, "Missile guidance by three-dimensional proportional navigation," *J. Appl. Phys.*, vol. 27, no. 5, p. 500, 1956.

[5] E. W. Justh and P. S. Krishnaprasad, "Steering laws for motion camouflage," *Proc. R. Soc. Lond. A, Math., Phys. Eng. Sci.*, vol. 462, no. 2076, pp. 3629–3643, Dec. 2006.

[6] E. Kreindler, "Optimality of proportional navigation," *AIAA J.*, vol. 11, no. 6, pp. 878–880, 1973.

[7] Y. B. Shtessel, I. A. Shkolnikov, and A. Levant, "Guidance and control of missile interceptor using second-order sliding modes," *IEEE Trans. Aerosp. Electron. Syst.*, vol. 45, no. 1, pp. 110–124, Jan. 2009.

[8] K. Ghose, T. K. Horiuchi, P. S. Krishnaprasad, and C. F. Moss, "Echolocating bats use a nearly time-optimal strategy to intercept prey," *PLoS Biol.*, vol. 4, no. 5, p. e108, May 2006.

[9] W. Scott and N. E. Leonard, "Pursuit, herding and evasion: A three-agent model of caribou predation," in *Proc. Amer. Control Conf. (ACC)*, 2013, pp. 2978–2983.

[10] R. M. Olberg, A. H. Worthington, and K. R. Venator, "Prey pursuit and interception in dragonflies," *J. Comparative Physiol. A, Neuroethol., Sensory, Neural, Behavioral Physiol.*, vol. 186, no. 2, pp. 155–162, 2000.

[11] A. Diabaté, A. S. Yaro, A. Dao, M. Diallo, D. L. Huestis, and T. Lehmann, "Spatial distribution and male mating success of *Anopheles gambiae* swarms," *BMC Evol. Biol.*, vol. 11, no. 1, p. 184, Jan. 2011.

[12] S. Butail, N. Manoukis, M. Diallo, J. M. Ribeiro, T. Lehmann, and D. A. Paley, "Reconstructing the flight kinematics of swarming and mating in wild mosquitoes," *J. Roy. Soc. Interface*, vol. 9, no. 75, pp. 2624–2638, 2012.

[13] D. Shishika and D. A. Paley, "Lyapunov stability analysis of a mosquito-inspired swarm model," in *Proc. 54th IEEE Conf. Decision Control (CDC)*, Dec. 2015, pp. 482–488.

[14] J. Moon, K. Kim, and Y. Kim, "Design of missile guidance law via variable structure control," *J. Guid., Control, Dyn.*, vol. 24, no. 4, pp. 659–664, Jul. 2001.

[15] T. Binazadeh and M.-J. Yazdanpanah, "Robust partial control design for non-linear control systems: A guidance application," *Proc. Inst. Mech. Eng. I, J. Syst. Control Eng.*, vol. 226, no. 2, pp. 233–242, Sep. 2012.

[16] R. Vidal, O. Shakernia, H. J. Kim, D. H. Shim, and S. Sastry, "Probabilistic pursuit–evasion games: Theory, implementation, and experimental evaluation," *IEEE Trans. Robot. Autom.*, vol. 18, no. 5, pp. 662–669, Oct. 2002.

[17] D. Shishika, J. K. Yim, and D. A. Paley, "Bio-inspired pursuit with autonomous hovercraft using Lyapunov-based control," in *Proc. Amer. Control Conf. (ACC)*, 2015, pp. 3107–3113.

[18] N. J. Kasdin and D. A. Paley, *Engineering Dynamics: A Comprehensive Introduction*. Princeton, NJ, USA: Princeton Univ. Press, 2011.

[19] H. K. Khalil and J. Grizzle, *Nonlinear Systems*. Upper Saddle River, NJ, USA: Prentice-Hall, 2002.

[20] K. Tanaka, M. Iwasaki, and H. O. Wang, "Switching control of an R/C hovercraft: Stabilization and smooth switching," *IEEE Trans. Syst., Man, Cybern. B, Cybern.*, vol. 31, no. 6, pp. 853–863, Dec. 2001.

[21] S. B. Fuller and R. M. Murray, "A hovercraft robot that uses insect-inspired visual autocorrelation for motion control in a corridor," in *Proc. IEEE Int. Conf. Robot. Biomimetics (ROBIO)*, Dec. 2011, pp. 1474–1481.

[22] F. L. Roubieu, J. Serres, N. Franceschini, F. Ruffier, and S. Viollet, "A fully-autonomous hovercraft inspired by bees: Wall following and speed control in straight and tapered corridors," in *Proc. IEEE Int. Conf. Robot. Biomimetics (ROBIO)*, Dec. 2012, pp. 1311–1318.

[23] C. Detweiler, B. Griffin, and H. Roehr, "Omni-directional hovercraft design as a foundation for MAV education," in *Proc. IEEE/RSJ Int. Conf. Intell. Robots Syst.*, Oct. 2012, pp. 786–792.

[24] A. Stubbs, V. Vladimerou, A. T. Fulford, D. King, J. Strick, and G. E. Dullerud, "Multivehicle systems control over networks: A hovercraft testbed for networked and decentralized control," *IEEE Control Syst. Mag.*, vol. 26, no. 3, pp. 56–69, Jun. 2006.

[25] C.-K. Ryoo, Y.-H. Kim, M.-J. Tahk, and K. Choi, "A missile guidance law based on Sontag's formula to intercept maneuvering targets," *Int. J. Control, Autom., Syst.*, vol. 5, no. 4, pp. 397–409, 2007.

[26] W.-H. Chen, "Nonlinear disturbance observer-enhanced dynamic inversion control of missiles," *J. Guid., Control, Dyn.*, vol. 26, no. 1, pp. 161–166, Jan. 2003.

[27] A. Levant, "Higher-order sliding modes, differentiation and output-feedback control," *Int. J. Control*, vol. 76, nos. 9–10, pp. 924–941, Jan. 2003.

[28] Y. Guo, S. Wang, Y. Yao, and B. Yang, "Evader maneuver on consideration of energy consumption in flight vehicle interception scenarios," *Aerosp. Sci. Technol.*, vol. 15, no. 7, pp. 519–525, 2011.

Daigo Shishika (S'13) received the B.S. degree in aerospace engineering from The University of Tokyo, Tokyo, Japan, in 2012, and the M.S. degree in aerospace engineering from the University of Maryland, College Park, MD, USA, in 2015, where he is currently pursuing the Ph.D. degree with the Aerospace Engineering Department.

His current research interests include flight dynamics and control, including pursuit evasion, collision avoidance, and collaborative control of autonomous vehicles inspired by animal group behaviors.

Justin K. Yim received the B.S. degree in mechanical engineering and electrical engineering and the M.S. degree in robotics from the University of Pennsylvania, Philadelphia, PA, USA, in 2015. He is currently pursuing the Ph.D. degree with the Electrical Engineering and Computer Sciences Department, University of California at Berkeley, Berkeley, CA, USA.

His current research interests include bioinspired robot mechanics and control.

Derek A. Paley (M'03–SM'11) received the B.S. degree in applied physics from Yale University, New Haven, CT, USA, in 1997, and the Ph.D. degree in mechanical and aerospace engineering from Princeton University, Princeton, NJ, USA, in 2007.

He is currently the Willis H. Young Jr. Associate Professor of Aerospace Engineering Education with the Department of Aerospace Engineering and the Institute for Systems Research, University of Maryland, College Park, MD, USA. His current research interests include dynamics and control, including cooperative control of autonomous vehicles, adaptive sampling with mobile networks, and spatial modeling of biological groups.

Dr. Paley is an Associate Fellow of the American Institute of Aeronautics and Astronautics (AIAA). He received the National Science Foundation CAREER Award in 2010, the Presidential Early Career Award for Scientists and Engineers in 2012, the University of Maryland E. Robert Kent Teaching Award for Junior Faculty Member in 2014, and the AIAA National Capital Section Engineer of the Year in 2015.